# Chemistry–A European Journal

## Supporting Information

## Surface Chemistry of a Halogenated Borazine: From Supramolecular Assemblies to a Random Covalent BN-Substituted Carbon Network

Birce Sena Tömekce, Marc G. Cuxart, Laura Caputo, Daniele Poletto, Jean-Christophe Charlier,* Davide Bonifazi,* and Willi Auwärter*

**SUPPORTING INFORMATION**

**Surface Chemistry of a Halogenated Borazine: From Supramolecular Assemblies to a Random Covalent BN-Substituted Carbon Network**

*Birce Sena Tömekce[1], Marc G. Cuxart[1], Laura Caputo[2], Daniele Poletto[3], Jean-Christophe Charlier\*[2], Davide Bonifazi\*[3] and Willi Auwärter\*[1]*

*[1]Physics Department E20, TUM School of Natural Sciences, Technical University of Munich, Garching, Germany*

*[2]Institute of Condensed Matter and Nanosciences, Université catholique de Louvain (UCLouvain), Belgium*

*[3]Institute of Organic Chemistry, Faculty of Chemistry, University of Vienna, Vienna, Austria*

# DFT METHODS AND MODELLING OF THE PRECURSOR

All spin-polarized calculations have been performed using density functional theory (DFT) with norm-conserving pseudopotentials as implemented in the Siesta code [1]. The generalized-gradient approximation of Perdew, Burke and Ernzherof (PBE) [2] has been exploited for the exchange-correlation density functional. A split-valence scheme has been used to generate a triple-zeta basis set that has been specifically optimized through comparison of structural and electronic properties across various benchmark systems computed using the ABINIT code [3]. Moreover, Van der Waals corrections are added adding Grimme corrections [4].

## Unreacted Tetrabromoborazine

Firstly, a structural comparison has been conducted among the potential configurations of the tetrabromoborazine monomer.
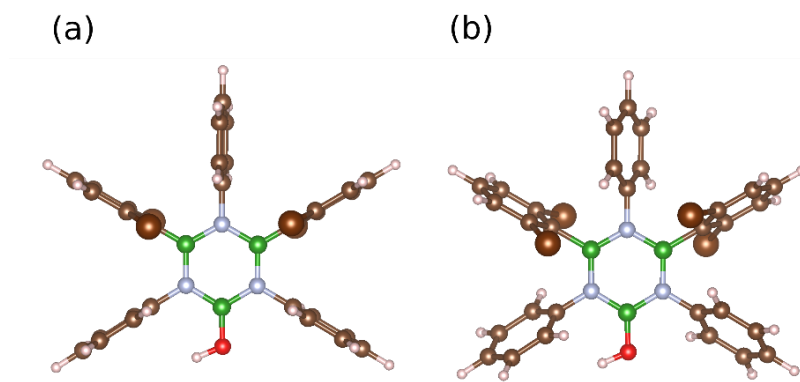


**Figure S1:** Two different configurations for the tetrabromo monomer containing (a) phenyl groups perpendicular to the plane of the molecule; (b) tilted phenyl groups. Carbon, Boron, Nitrogen, Oxygen, Hydrogen and Bromine are represented with brown, green, gray, red, white spheres and dark-brown larger spheres, respectively.

The configurations depicted in **Fig. S1** have undergone geometric optimization. Notably, the two configurations have comparable energy ($\Delta E \sim 3$meV/atom). Therefore, these two configurations could exist within the system. The phenyl groups have some rotational freedom and this flexibility allows for dynamic adjustments and reorientations upon surface adsorption, enabling various configurations to be present simultaneously.

## ADDITIONAL EXPERIMENTAL DATA AND ANALYSIS

### dI/dV Spectroscopy

**Figure S2** compares dI/dV spectra for a bare Ag(111) area, a supramolecular island of intact tetrabromoborazine, and the random covalent network. The step-like features are assigned to the surface state of Ag(111), which is upshifted by the adsorbed molecules / the network, as similarly reported for different adsorbates on Ag(111) [5], [6].
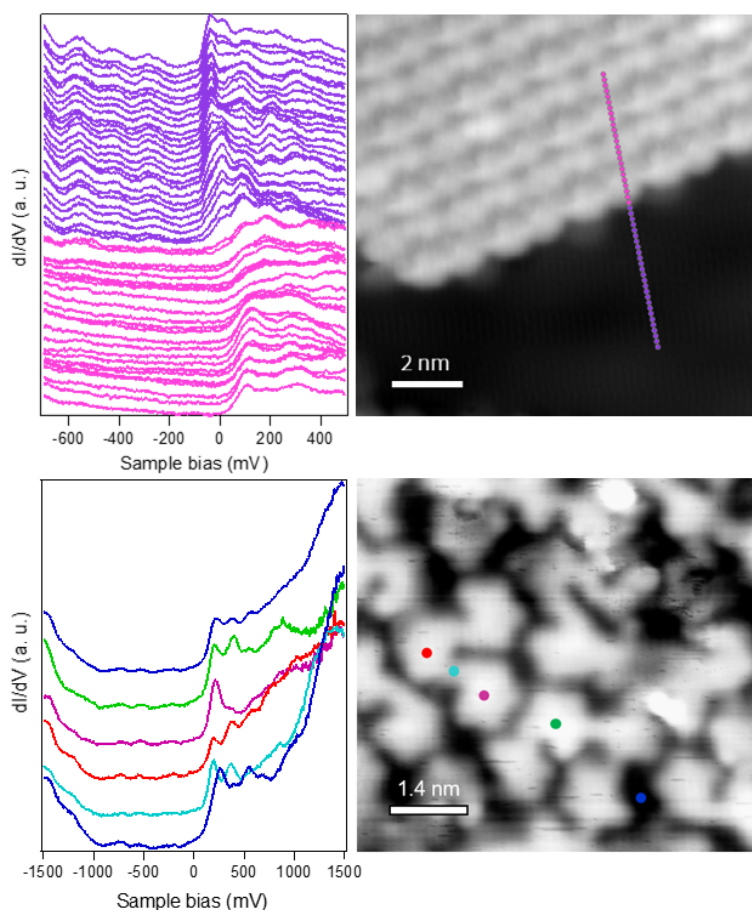


**Figure S2:** (Top) dI/dV spectra measured along a line show the evolution of the Ag(111) surface state. On the bare Ag(111) area (purple), the onset occurs around -67 meV. On the tetrabromoborazine island (pink), it is upshifted by about 130 meV. (Bottom) dI/dV spectra measured at positions indicated by the colored markers in the STM topography image of the covalent network, revealing the upshifted surface state. ($V_b$: 1500 mV, $I_t$: 0.49 nA, lock-in modulation amplitude: 50 mV)

## Hexagonal Phase
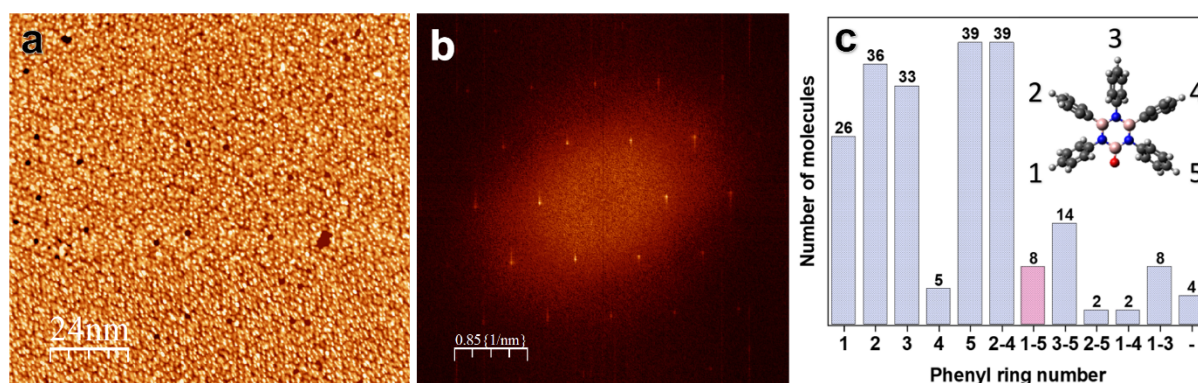


**Figure S3:** (a) Large scale STM image of the hexagonal phase prepared by annealing at 170°C and (b) its 2D-FFT image confirming hexagonal symmetry. (c) Histogram showing the statistics of the tilted phenyl rings of the monomers counted from the STM image in **Figure 2c**. (-) refers to completely planarized molecules.

## Kagomé Phase and Dimers
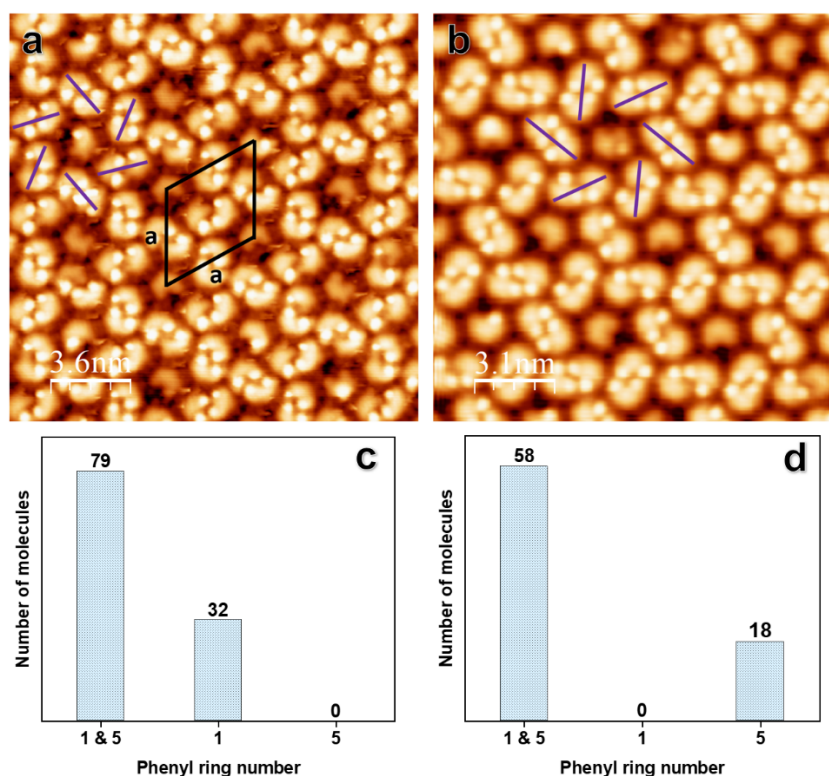


**Figure S4:** Different kagomé phase domains observed after annealing at 220°C, revealing (a) counter-clockwise chirality and (b) clockwise chirality, respectively. Histograms for the two chiralities are provided in panels (c) and (d) below.

**C 1s and N 1s XPS**

**Figure S5** shows the C 1s and N 1s XPS data after low temperature deposition (green spectra) and annealing to room temperature (blue) and higher temperatures. The initial shift towards lower binding energy, concomitant with debromination and dehydrogenation (see **Figure 4**), is attributed to increased molecule - substrate interactions [7]. From room temperature up to 410°C, the N 1s and C 1s core level spectra show gradual peak shifts towards higher binding energy. This observation is in line with the findings of a comparative study on $B_3N_3$-doped hexa-peri-hexabenzocoronene (BN-HBC), its half-planarized analogue $B_3N_3$-hexabenzotri-phenylen-2H (BN-HBP-2H), and propeller-like $B_3N_3$-hexabenzo-triphenylene (BN-HBP) [8]. For N 1s, this trend was attributed to a change in polarity of the BN bond and interaction of the BN core with the substrate, as the molecules flatten and couple covalently. Note that the N 1s peak broadens with increasing annealing temperature. The FWHM values are 1.3 eV at room temperature, 1.5 eV after annealing at 220°C and 320°C, and 1.8 eV after annealing at 410°C. This indicates the presence of multiple contributions with similar binding energies, which might originate from the byproducts observed in the STM data (see **Figure 3a**). In C 1s spectra, a shoulder around 286.2 eV can be noticed after high temperature annealing, specifically at 410°C. This is likely due to the C-O bonding [9], [10] arising from random intermolecular coupling.
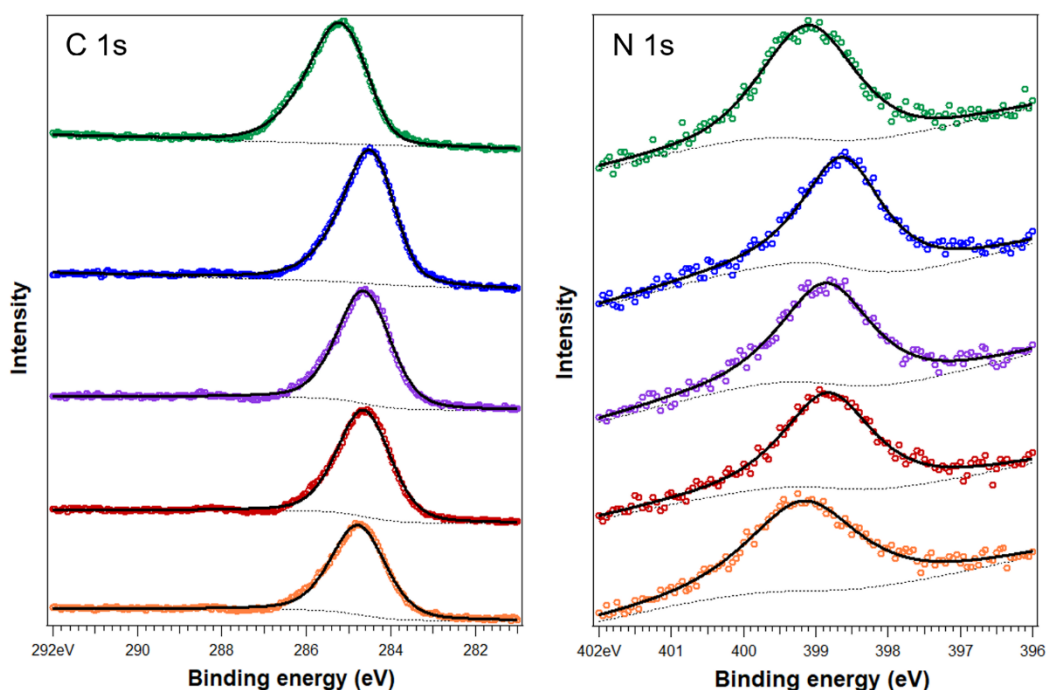


**Figure S5:** XP C 1s and N 1s core level spectra measured at -50°C (green), room temperature (blue), and after annealing to 220°C (purple), 320°C (red), and 410°C (orange).
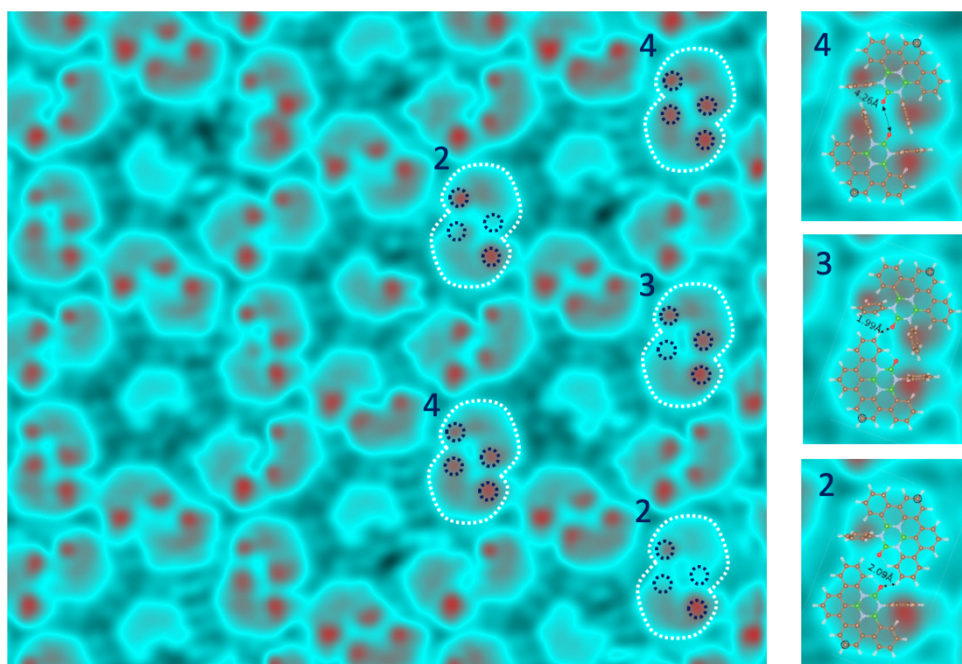
**Figure S6:** STM image of the kagomé phase represented in a false colour plot to emphasize the molecular outlines (visible in bright cyan) and the protrusions attributed to tilted terminal phenyl rings (red, largest apparent heights). Note that irrespective of the number of tilted terminal rings per dimer (2, 3 or 4, see numbers in image), the outline of the dimers and thus the lateral positioning of the two constituting molecules is very similar. This is visualized by superimposing the outline (white dotted line) and protrusions (blue dotted lines) optimized for the dimer on the top right to four other dimers with identical orientation. Dimers rotated by 60° or 120° show slight variations in the outline, attributed to tip asymmetries. The column on the right shows the DFT Model 1 (top), 2 (middle), and 3 (bottom) superimposed on the STM data (see **Figure S11** for further details).
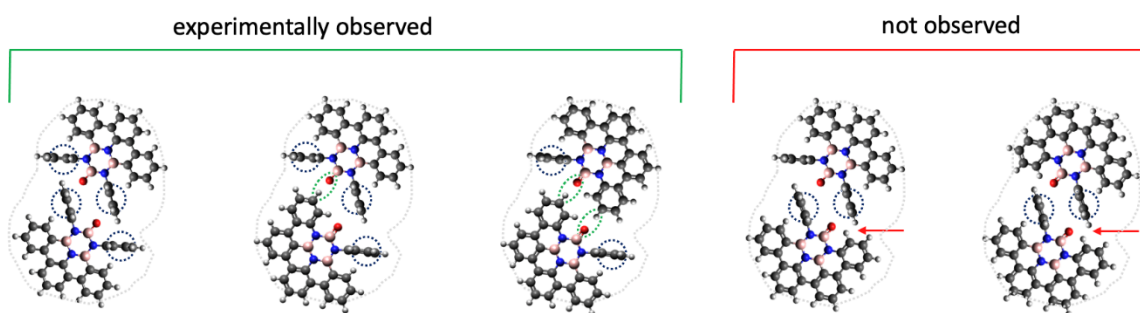


**Figure S7:** Schematic dimer models for monomers with two tilted terminal groups, one tilted terminal groups and zero or one fused terminal group. Tilted terminal groups (1, 5) are highlighted by dashed circles. The left three configurations, presumably stabilized by hydrogen bonding (dashed green ellipses), are observed experimentally. The two configurations on the right, are not observed. Red arrows point to sterically crowded areas.

## DFT OPTIMIZATION OF DIMERS

In the experimental setup, molecules that self-assembly to form dimers are constrained to a planar configuration owing to the presence of the substrate. In our calculations, the explicit inclusion of the substrate is restricted by computational limitations. However, we mimic this scenario by permitting the conjugated C-sp$^2$ portion of the molecules to undergo geometric relaxation solely in two dimensions, while maintaining the atomic coordinates fixed along the direction perpendicular to the substrate plane.

Subsequently, the formation of dimers was investigated by freely approaching two monomers depicted in **Scheme 1(C)** while allowing their conjugated part to relax only in 2D. Specifically, we examined both the fully saturated dimer (**Fig. S8**) and the dehydrogenated cases, where one (**Fig. S9**) or both monomers (**Fig. S10**) experienced hydrogen removal in the hydroxyl group.
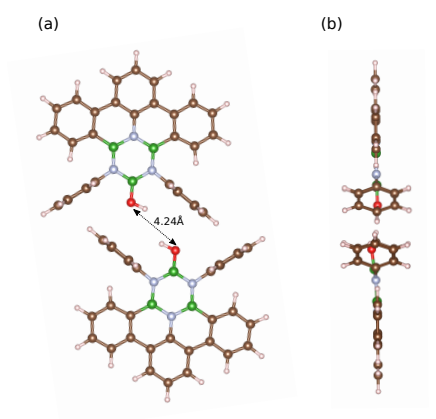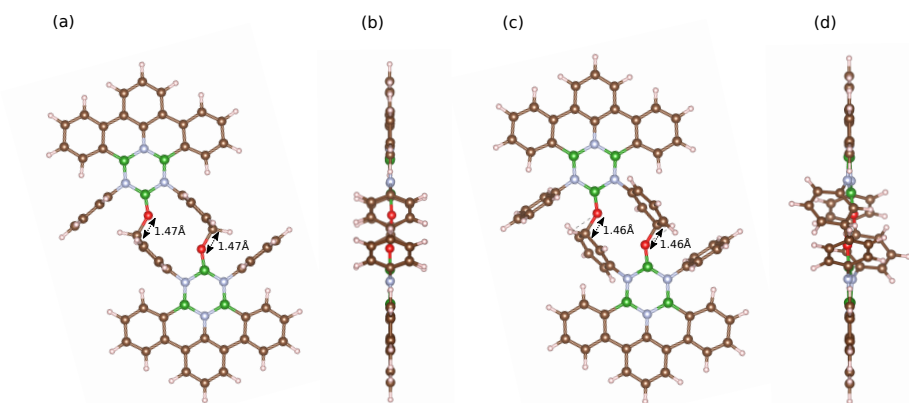


**Figure S8**: Atomistic model of fully saturated dimer from the (a) top view and (b) side view.
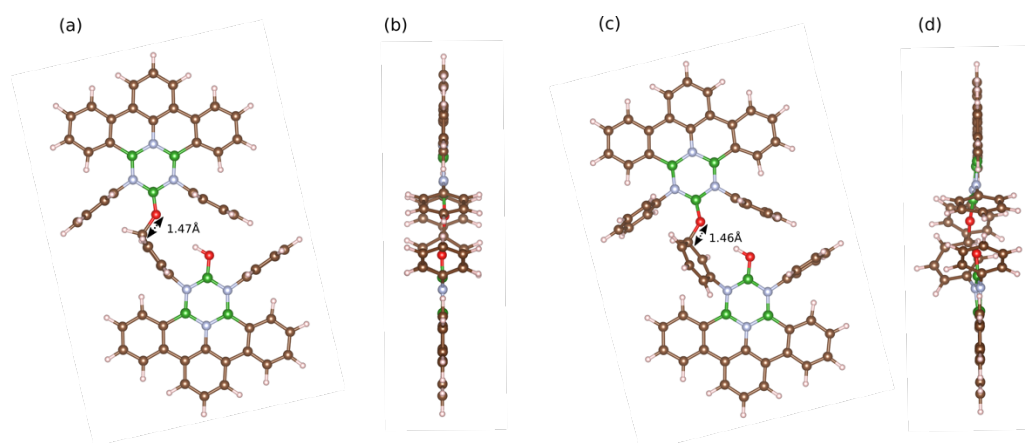


**Figure S9:** Atomistic models of single dehydrogenated dimers with perpendicular bonding phenyl groups seen from the (a) top view and (b) side view; and with tilted bonding phenyl group seen from the (c) top view and (d) side view.
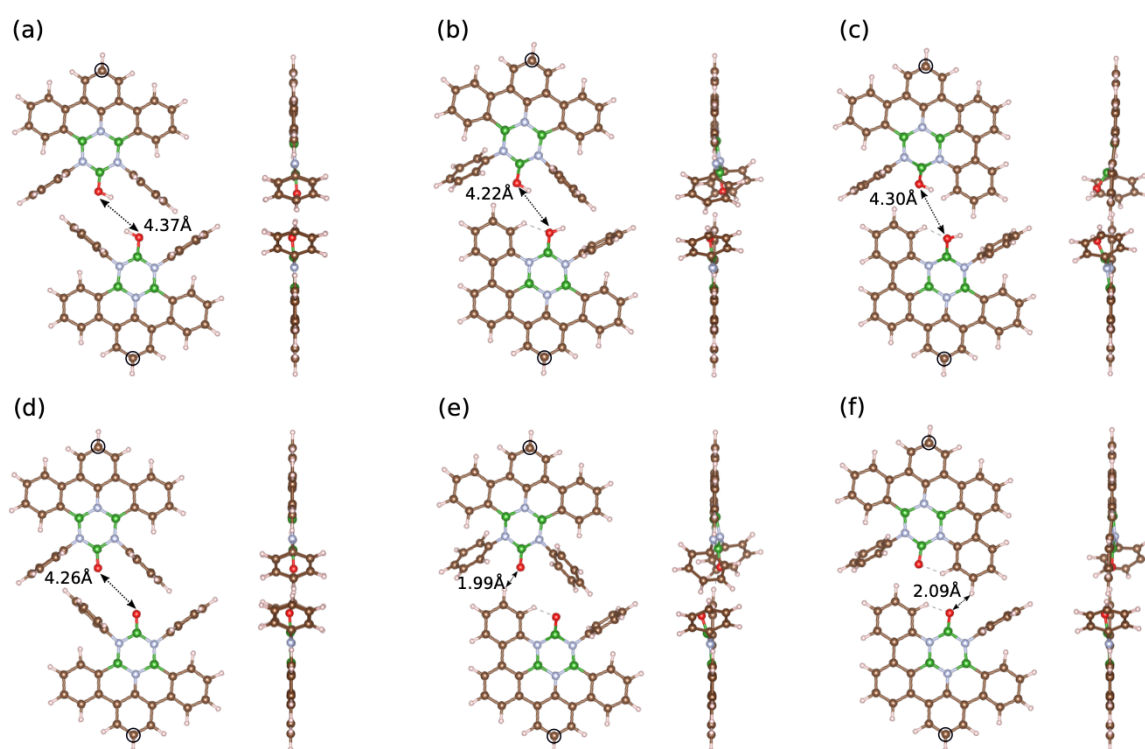
**Figure S10:** Atomistic models of doubly dehydrogenated models with perpendicular bonding phenyl groups seen from the (a) top view and (b) side view; and with tilted bonding phenyl groups seen from the (c) top view and (d) side view.

For the dimer having both the OH group intact, reported in **Fig. S8**, the distance between oxygen atoms is 4.24 Å. Nevertheless, the perpendicular geometry and 2.6 Å distance between C and H atoms of the opposing phenyl rings suggest a potential presence of CH/π interaction [11]. In the single dehydrogenated case, reported in **Fig. S9**, one of the phenyl rings forms a C-O bond (1.47 Å) in $sp^3$ configuration with $O^-$. In this case, two possible configurations are reported. In the first case (**Fig. S9 a,b**), the bonding phenyl is perpendicular to the molecular plane but the bonded geometry induces a slight distortion in molecular axis. In the second configuration (**Fig. S9 c,d**), the bonding phenyl is tilted with an angle of 66° with respect to the molecular plane, accompanied by a reduced O-O distance of 3.73 Å. Remarkably, the energy difference between the two configurations is less than 1 meV/atom. The doubly dehydrogenated configuration, reported in **Fig. S10**, follows the same trend; forming two C-O bonds by the opposite phenyl rings. Similarly, two different configurations have been examined, mirroring the cases reported for the singly dehydrogenated states. In this case, the difference in energy between the doubly dehydrogenated configurations is around 2 meV/atom. Consequently, in both monomer and dimer calculations, the differences in energies are particularly marginal. Additionally, the substrate is not explicitly considered which could potentially affect the stability of the models studied, underscoring the potential difficulty in distinguish them on the surface.

Indeed, the formation of covalent bonding between the two monomers might be facilitated by the formation of radical oxygens following the hydrogen removal. This, coupled with the absence of charge redistribution due to the lack of substrate in our calculations, could serve as a significant driving force for the monomers, and in particular the dehydrogenated cases, to

approach. To circumvent this limitation, studies focusing on the experimentally suggested supramolecular dimers reported in **Fig. S7** have been conducted by maintaining a fixed distance between the two monomers. This was achieved by completely freezing the carbon atoms furthest from the hydroxyl groups during the geometry optimization. In **Fig. S11**, the optimized dimers are depicted, with the latter carbon atoms circled in black for clarity. Specifically, the fully saturated model will be referred as model 1, the dimer with one half-planarized monomer as model 2, and the dimer with two half-planarized monomers as model 3. For each case, the doubly dehydrogenated cases are studied alongside the saturated models.



**Figure S11:** Atomistic models for three different experimentally observed models, viewed from the top and side view. (a) fully saturated configuration (model 1) and (d) the correspondent doubly dehydrogenated case; (b) half-planarized configuration (model 2) and (e) the correspondent doubly dehydrogenated case; (c) planarized dimer (model 3) and (f) the correspondent doubly dehydrogenated case. The carbons circled with black lines are completely fixed in geometry optimization.

Consequently, with the fixed distance, the covalent bonding is no longer present in the doubly dehydrogenated case of model 1. The covalent intermolecular bond formation predicted by DFT in absence of a substrate and not fixing the distance (**Figures S9 and S10**) might be realized in an experimental setting employing non-metallic supports, such as dielectric spacer layers.
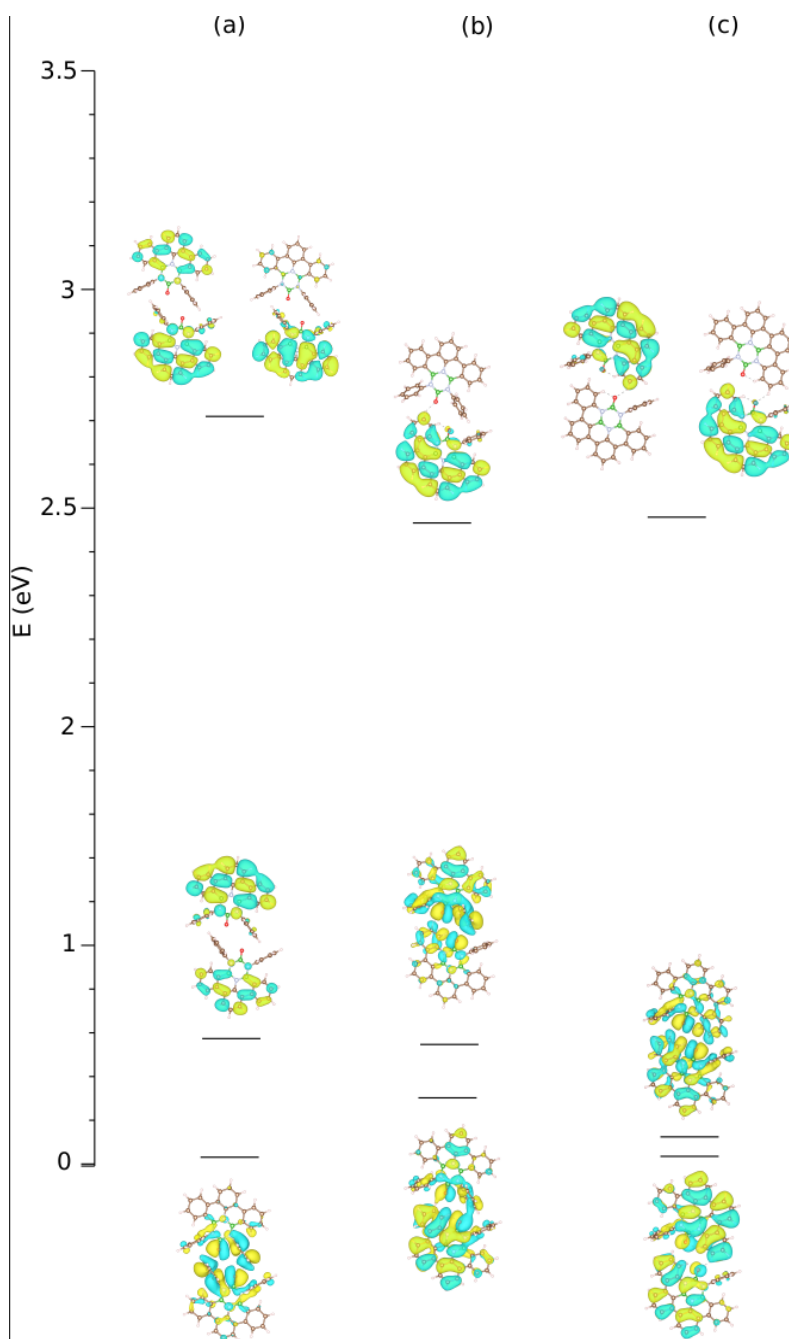
Lastly, the LUMO, LUMO+1 and LUMO+2 orbitals for models 1,2 and 3 have been computed as a comparison with the experimental dI/dV maps. Due to the radical formation on the oxygen atoms of the two dimers that might lead to spin polarized midgap states, the LUMOs are initially presented for the fully saturated cases **(Fig. S6)**. From this point onward, states depicted at the same energy levels in the images exhibit an energy difference equal to or less than 0.03 eV.
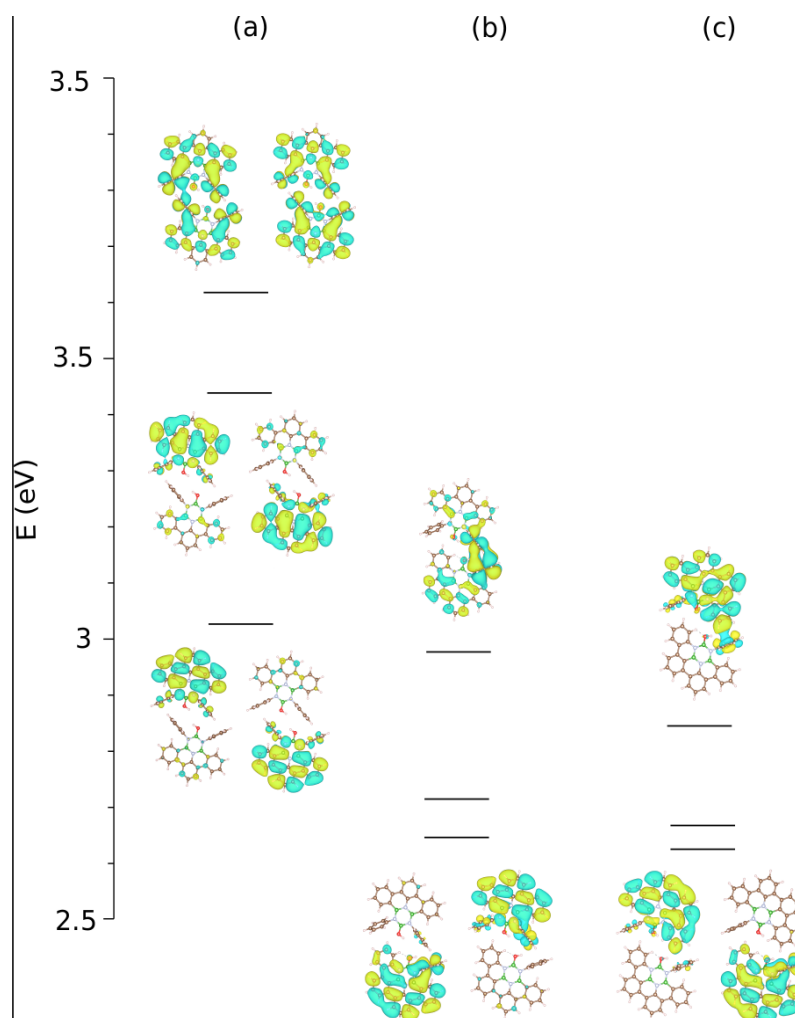


**Figure S12:** LUMO, LUMO+1 and LUMO+2 orbitals for (a) model 1, (b) model 2 and (c) model 3. The energy has been normalized for the HOMO level to be zero. Each plot has been obtained with an isosurface value of 0.009 e/Å$^3$. The yellow (blue) surface represents the positive (negative) values of the wavefunction.

In all instances, the LUMO and LUMO+1 orbitals exhibit delocalization across the entire structure. Consequently, even if structurally not equivalent to experiments, these configurations describe the delocalization of the LUMO. Moreover, the LUMO+2 maintains a delocalized nature while also showing some localized charge density between the two monomers, indicating the presence of CH/π interactions, particularly in Model b and c. For further comparison to the

experiment, the LUMO, LUMO+1 and LUMO+2 orbitals of the dehydrogenated cases for Model 1, 2 and 3 are reported in **Figure S7**. For the dehydrogenated models, the formation of spin-polarized structures results in the emergence of mid gap states, which now represent LUMO and LUMO+1, exhibiting high local charge density between the two monomers. However, upon examining the higher energy states (LUMO+2), one can recognize a very similar character to the LUMO nature of the fully saturated models.



**Figure S13:** LUMO, LUMO+1 and LUMO+2 orbitals for (a) Model 1, (b) Model 2, (c) Model 3 in the dehydrogenated configurations.

## BIAS DEPENDENT STM IMAGING
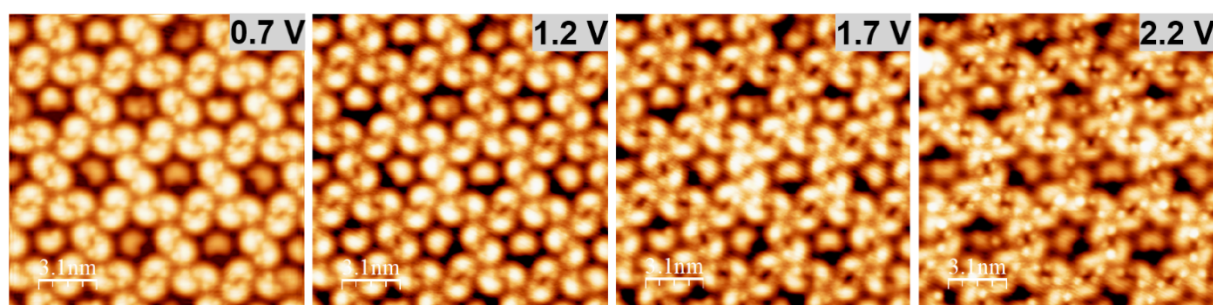


**Figure S14:** Bias dependent STM images of the kagomé phase obtained from the same area.

## SYNTHESIS OF TETRABROMOBORAZINE

**Materials and Methods**. All synthetic manipulations of air-sensitive compounds were carried out under an argon atmosphere using standard Schlenk techniques or in an argon-filled MBraun glovebox ($O_2$ and $H_2O$ levels below 1.0 ppm). Glassware was dried overnight in a hot oven (120 °C) and heated under vacuum before use. Toluene, $CH_2Cl_2$, and THF were dried using a MBraun solvent purification system, stored in Straus flasks over activated 3 Å molecular sieves, and were freeze-pump-thaw degassed prior to use. Anhydrous 1,4-dioxane, chlorobenzene, cyclohexane, 1,2-dichloroethane and 2-methyltetrahydrofuran (MeTHF) were purchased from Sigma-Aldrich or Acros Organics and transferred into Straus flasks containing activated 3 Å molecular sieves, and were freeze-pump-thaw degassed prior to use. *t*BuONa was heated at 120 °C under reduced pressure ($1 \times 10^{-2}$ mbar) for at least 8 h and stored in the glovebox. All other compounds were purchased from commercial vendors and used as received (e.g., Sigma-Aldrich, TCI, BLD Pharm, Fluorochem, Fisher Scientific, ABCR, Acros Organics, Strem). Room (ambient) temperature (RT) refers to 24 °C (± 1 °C).

**Melting points** (mp) were measured on a Leica Galen III microscope equipped with a heating block and a Hg thermometer ($T_{max}$ = 200 °C) on a microscope slide, under air, and are uncorrected. According to the limitations of the apparatus, the compounds which did not melt or that decompose (dec) up to 200 °C are presented as "> 200 °C".

**Nuclear magnetic resonance** (NMR) characterizations were performed at the NMR centre of the University of Vienna. All NMR spectra were recorded on a 400 Bruker AV Neo ($^1$H, 400 MHz; $^{13}$C, 100.6 MHz), 500 Bruker AV Neo ($^1$H, 500 MHz; $^{13}$C, 125.8 MHz), a 600 Bruker AV III ($^1$H, 600 MHz; $^{13}$C, 150.9 MHz) or a 700 Bruker Avance Neo ($^1$H, 700 MHz; $^{13}$C, 176.1 MHz) Spectrometers. Carbon spectra were recorded with a complete decoupling for the proton. Proton and carbon chemical shifts are reported in parts per million (ppm, $\delta$ scale) according to tetramethylsilane ($\delta_H = \delta_C = 0$ ppm) using the solvent residual signal as an internal reference (e.g., CHCl$_3$: $\delta_H = 7.26$ ppm, $\delta_C = 77.16$ ppm). Boron chemical shifts are reported in ppm, referenced to the external standard boron signal of BF$_3$·Et$_2$O ($\delta_B = 0$ ppm). All coupling constants (*J*) are reported in Hz. Multiplicity of signals are indicated as "s", "d", "dd", "ddd", "t", "q", "p", "h", "m" for singlet, doublet, doublet of doublets, doublet of doublets of doublets,

triplet, quartet, pentet, heptet and multiplet, respectively. Unless otherwise stated all NMR spectra are recorded at 293 K.

**Infrared Spectra** (IR) were recorded on a Bruker Alpha FT-IR spectrometer in ATR mode. Selected absorption bands are reported in wavenumbers (cm$^{-1}$).

**MALDI-TOF Analysis**. High-resolution MALDI-TOF MS analyses were performed using a Bruker timsTOF fleX ESI/MALDI dual source - trapped ion mobility separation - Qq-TOF mass spectrometer in positive ion mode. The sum formulas of the detected ions were determined using Bruker Compass DataAnalysis 5.3 based on the mass accuracy ($\Delta$m/z $\leq$ 5 ppm) and isotopic pattern matching (SmartFormula algorithm). One microliter of a solution of the matrix (*trans*-2-[3-(4-*t*-butyl-phenyl)-2-methyl-2-propenylidene]malonitrile, DCTB) in THF (10 mg/mL) was spotted onto a well of the MALDI plate, and the solvent was allowed to evaporate. Sample solutions (1 mg/mL in THF) were prepared, and 1 μL of this solution was spotted onto the well by a layering method. The solvent was evaporated prior to analysis. Data were collected in positive polarity mode.

***B,B'*-Bis(2,6-dibromophenyl)-*B''*-hydroxy-*N,N',N''*-triphenylborazine**
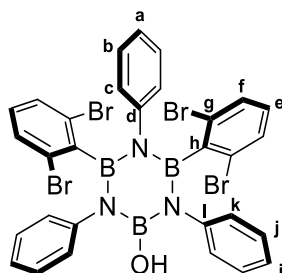


**Mixture A**: In a glove box, a Schlenk tube equipped with rubber septum was loaded with aniline (0.29 mL, 0.30 g, 3.2 mmol) and toluene (6 mL). The mixture was cooled at 0 °C using an ice bath (meanwhile the closed flask was brought outside the glovebox). Upon strong stirring, BCl$_3$ (1 M in heptane, 4 mL, 4 mmol) was then added to the mixture dropwise. The rubber septum was rapidly exchanged with an oven-dried condenser under Argon flow. The top of the condenser was equipped with an oven-dried bubbler filled with H$_2$SO$_4$ (97%). The reaction mixture was stirred for 18 h at 120 °C under constant Argon flow. The mixture was then allowed to reach rt and, under Argon flow, the condenser exchanged with an oven-dried glass stopper. The solvent was removed *in vacuo* affording a white solid. The vessel was transferred into a glove box, and the solid re-dissolved in 2-methyltetrahydrofuran (MeTHF, 8 mL).

**Mixture B**: In a glove box, 1,3-dibromo-2-iodobenzene (1.28 g, 3.54 mmol) and 2-methyltetrahydrofuran (8 mL) were added in a Schlenk tube equipped with a septum. The mixture was cooled at -131 °C with a pentane/N$_2$(*l*) bath (meanwhile the closed flask was

brought outside the glovebox). *n*BuLi (2.5 M in hexanes, 1.5 mL, 3.75 mmol) was added dropwise. The mixture was kept stirring at -131 °C for 0.5 h.

**Mixture C**: Mixture A (at rt) was cannulated dropwise on the vessel containing mixture B (freshly prepared, at -131 °C). The reaction was kept at -131 °C for 0.5 h, then allowed to warm to -98 °C with a MeOH/N$_2$(*l*) bath for 0.5 h, and finally allowed to reach rt overnight. After 18 h the mixture was quenched with water and extracted with EtOAc (3-x 100 mL). The organic layers were combined, washed with brine (100 mL) and dried over MgSO$_4$. The solvents were removed *in vacuo*, affording a brown solid. The solid was re-dissolved in CH$_2$Cl$_2$ and precipitated in methanol, affording the desired compound as a white powder (452 mg, 0.570 mmol, 53%). An analytical sample of the compound was further purified by recrystallization from a CH$_3$CN/CH$_2$Cl$_2$ solvent mixture mp: 287-290 °C. $^1$H NMR (600 MHz, CDCl$_3$) δ 7.59 (d, *J* = 7.4 Hz, 2H, H$_c$), 7.46 (d, *J* = 7.6 Hz, 4H, H$_k$), 7.19 (t, *J* = 7.6 Hz, 4H, H$_j$), 7.06 (m, 6H, H$_i$ + H$_f$), 6.87 (t, *J* = 7.4 Hz, 2H, H$_b$), 6.80 (t, *J* = 7.4 Hz, 1H, H$_a$), 6.63 (t, *J* = 7.9 Hz, 2H, H$_e$), 3.59 (s, 1H, B-OH). $^{13}$C NMR (151 MHz, CDCl$_3$) δ 144.7 (C$_d$), 143.0 (C$_l$), 130.0 (C$_e$), 129.7 (C$_f$), 128.4 (C$_j$), 127.7 (C$_k$), 127.2 (C$_c$), 126.9 (C$_b$), 126.1 (C$_g$), 125.9 (C$_i$), 125.2 (C$_a$) (1 signal missing due to $^{11}$B quadrupolar relaxation). $^{11}$B NMR (193 MHz, CDCl$_3$) δ 34.3, 25.2. IR (cm$^{-1}$): 3565, 3026, 1541, 1490, 1454, 1430, 1398, 1379, 1205, 1138, 1047, 1028, 911, 770, 752, 708, 696, 550.  HRMS (MALDI): m/z calcd for [C$_{30}$H$_{22}$B$_3$N$_3$Br$_4$O]$^+$: 792.8742 [M]$^+$; found: 792.8760.
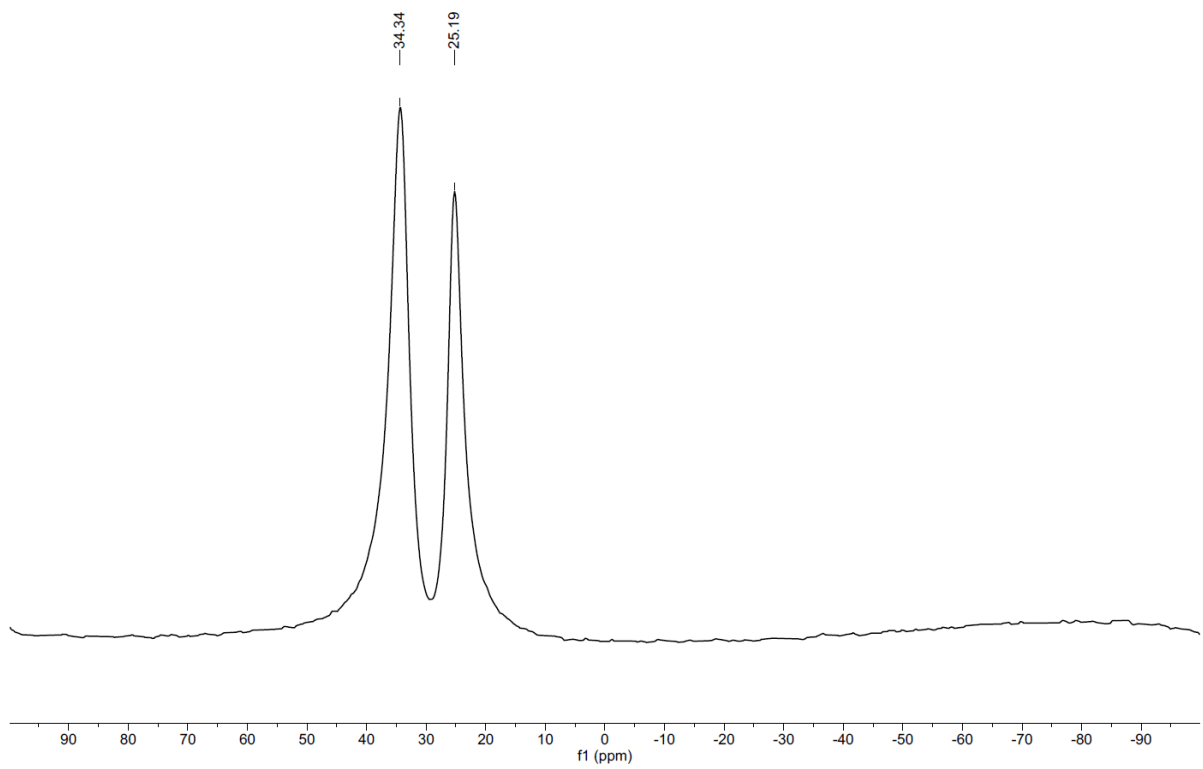
1,3-Dibromo-2-iodobenzene
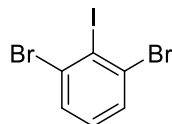


A flame-dried Schlenk tube equipped with rubber septum was loaded with 1,3-dibromobenzene (0.26 mL, 0.50 g, 2.1 mmol, freshly distilled from CaH$_2$) and dry THF (8 mL). The resulting mixture was cooled to  -78 °C with an acetone/dry ice bath, and lithium diisopropylamide (1 M in hexanes, 2.5 mL, 2.5 mmol) was added dropwise. The reaction was kept stirring at -78 °C for 2 h (mixture A). In parallel, a flame-dried Schlenk tube was loaded with I$_2$ (600 mg, 2.54 mmol) and dry tetrahydrofuran (6 mL) (mixture B). Mixture B (at rt) was then cannulated to mixture A (at -78 °C). The reaction was kept stirring at -78 °C for 5 min and allowed to reach rt. The reaction was then quenched with Na$_2$S$_2$O$_3$ (1 M in H$_2$O, 20 mL, 20 mmol) and extracted with Et$_2$O (3 x 50 mL). The combined organic layers were washed with brine (50 mL) and dried over MgSO$_4$. The solvent was removed *in vacuo* affording a yellow solid, which was recrystallized from EtOH/H$_2$O 25:1 to get the desired compound as a white crystalline solid (645 mg, 1.783 mmol, 82%). $^1$H NMR (600 MHz, CDCl$_3$) δ 7.55 (d, J = 8.0 Hz, 2H), 7.07 (t, J = 8.0 Hz, 1H). $^{13}$C NMR (151 MHz, CDCl$_3$) δ 131.5, 131.2, 130.5, 109.5. HRMS (GC/Q-TOF): m/z calcd for [C$_6$H$_3$Br$_2$I]$^+$: 361.7626 [M]$^+$; found: 361.7643
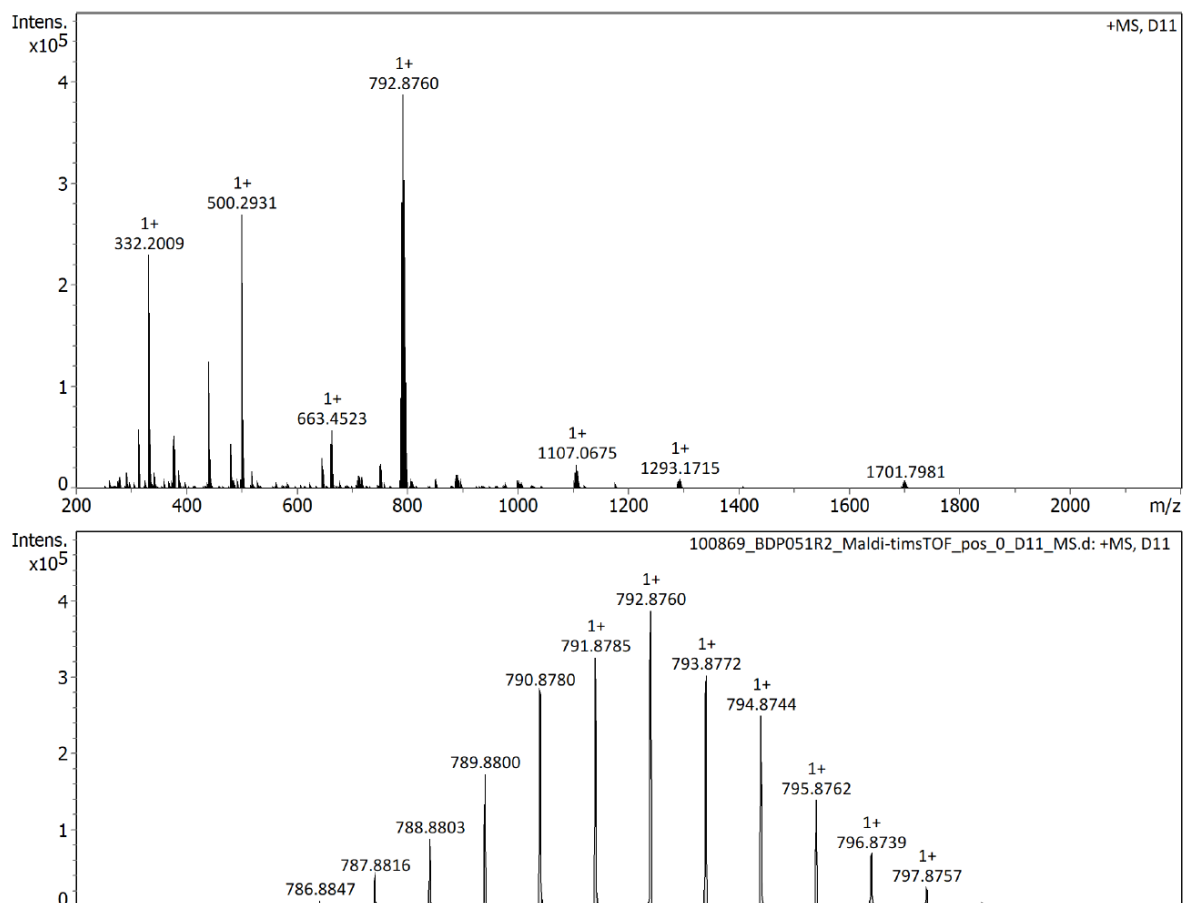
# NMR and HRMS spectra
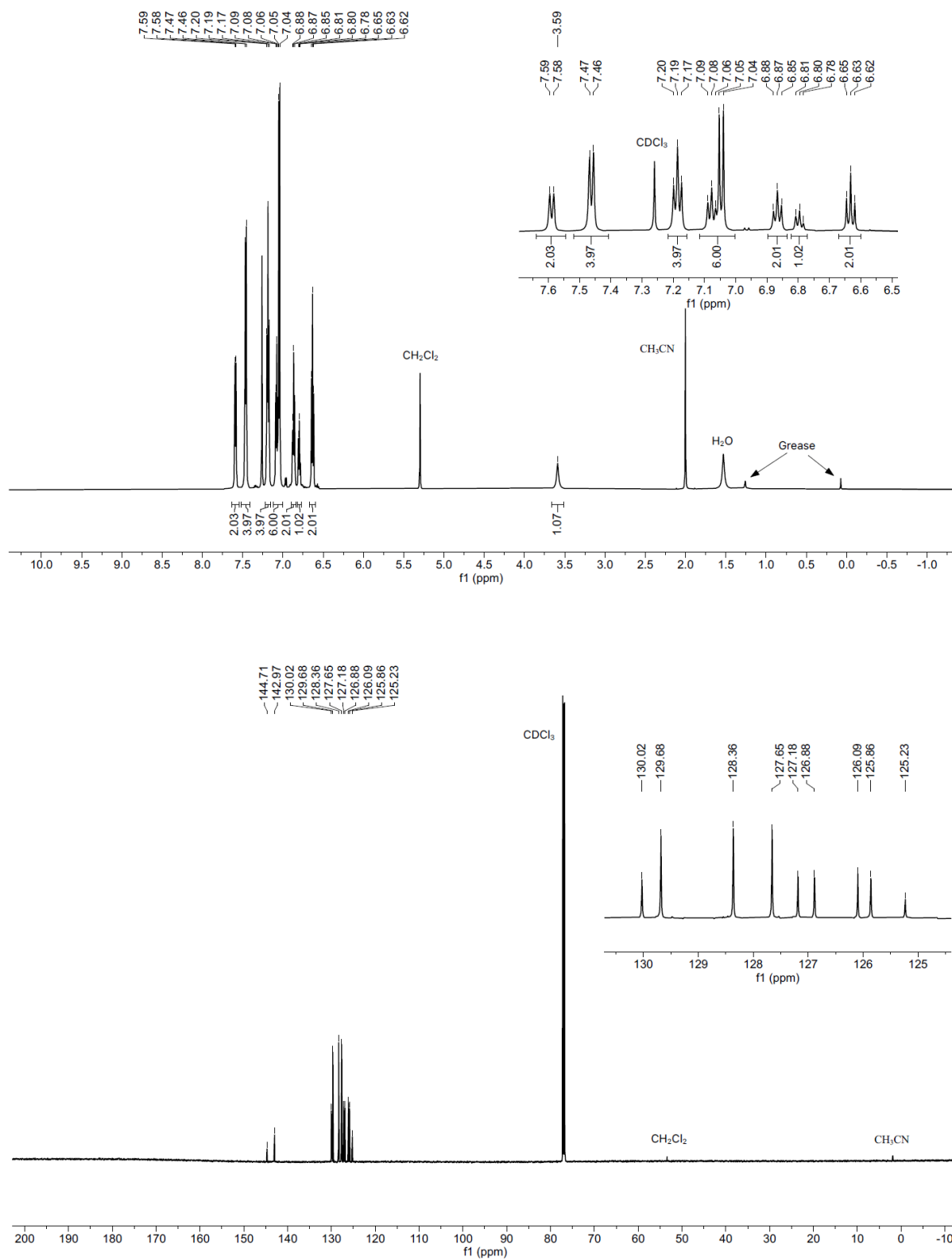


**Figure S15**: $^1$H (top) and $^{13}$C{$^1$H} (bottom) NMR spectra (CDCl$_3$) of **tetrabromoborazine** (residual solvents are present).
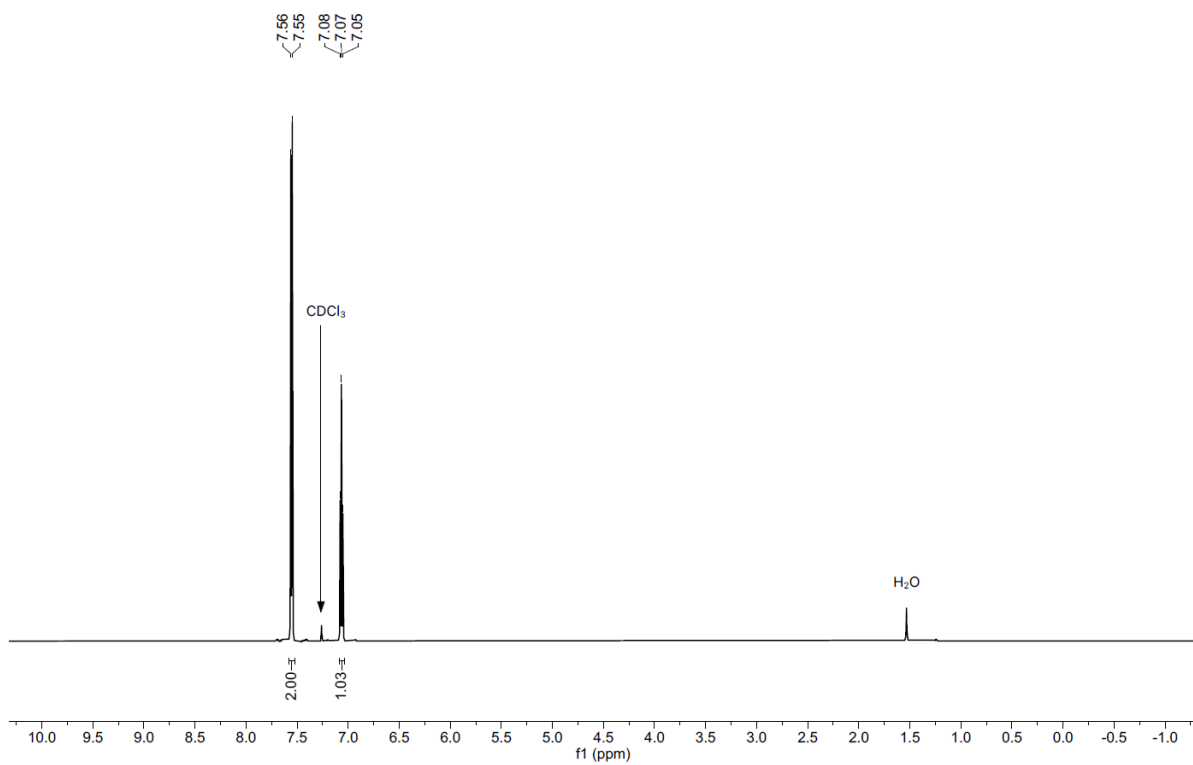
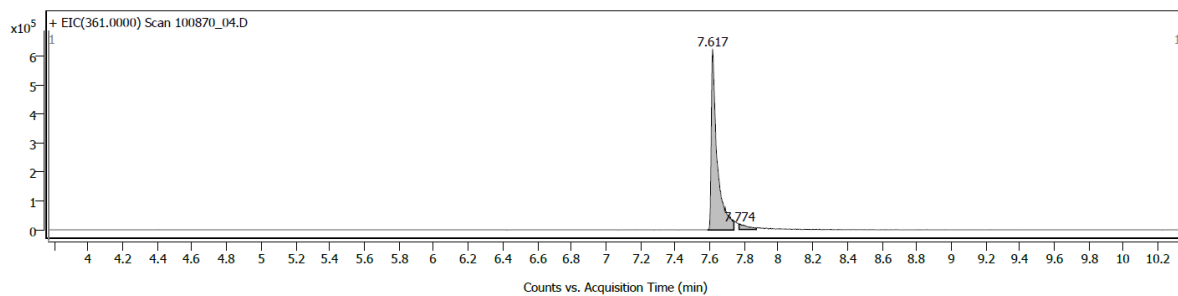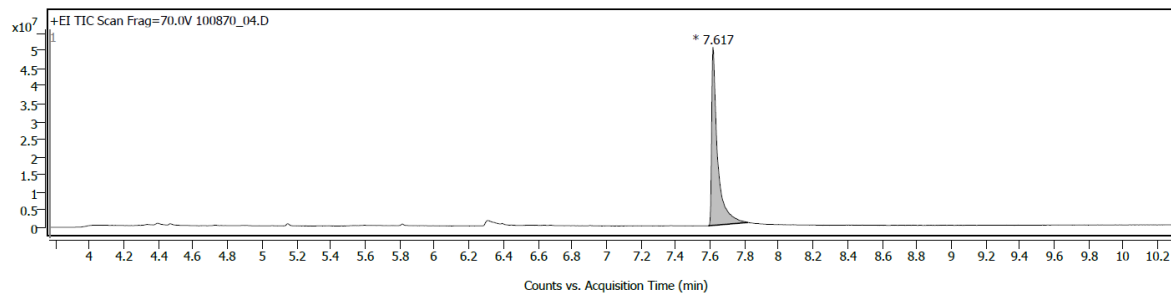**Figure S16**: $^{13}$B NMR spectra (CDCl$_3$) of **tetrabromoborazine**.

**Figure S17**: HRMS (MALDI) spectrometry analysis for **tetrabromoborazine**.
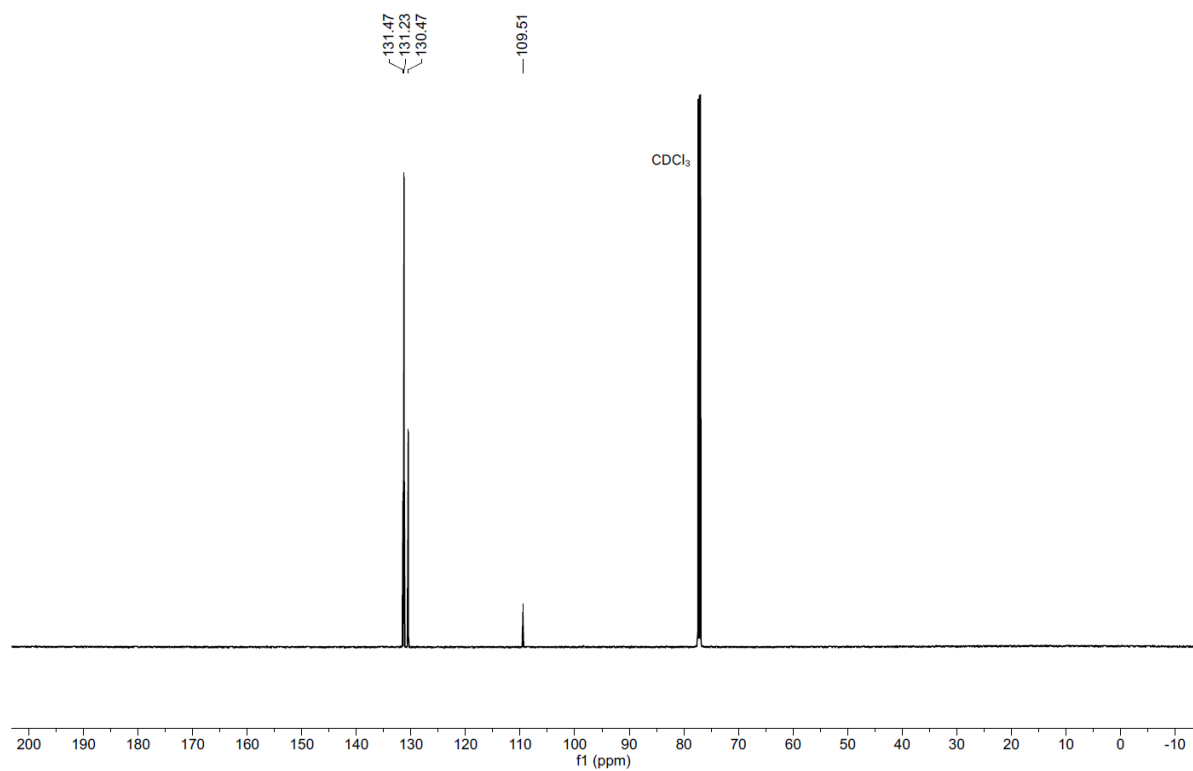
**Figure S18**: ¹H (top) and ¹³C{¹H} (bottom) NMR spectra (CDCl₃) of 1,3-dibromo-2-iodobenzene.

**Sample Chromatograms**



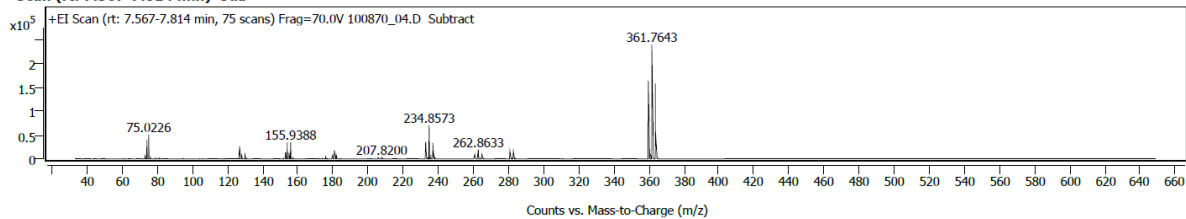**Sample Spectra**

**+ Scan (rt: 7.567-7.814 min) Sub**



**Figure S19**: HRMS (GC/Q-TOF) spectrometric analysis for 1,3-dibromo-2-iodobenzene.

# REFERENCES

[1]   J. M. Soler, E. Artacho, J. D. Gale, A. García, J. Junquera, P. Ordejón, D. Sánchez-Portal, *J. Phys. Condens. Matter.* **2002**, *14*, 2745–2779.

[2]   J. P. Perdew, K. Burke, M. Ernzerhof, *Phys. Rev. Lett.* **1996**, *77*, 3865–3868.

[3]   X. Gonze, B. Amadon, G. Antonius, F. Arnardi, L. Baguet, J. M. Beuken, J. Bieder, F. Bottin, J. Bouchet, E. Bousquet, N. Brouwer, F. Bruneval, G. Brunin, T. Cavignac, J. B. Charraud, W. Chen, M. Côté, S. Cottenier, J. Denier, G. Geneste, P. Ghosez, M. Giantomassi, Y. Gillet, O. Gingras, D. R. Hamann, G. Hautier, X. He, N. Helbig, N. Holzwarth, Y. Jia, F. Jollet, W. Lafargue-Dit-Hauret, K. Lejaeghere, M. A. L. Marques, A. Martin, C. Martins, H. P. C. Miranda, F. Naccarato, K. Persson, G. Petretto, V. Planes, Y. Pouillon, S. Prokhorenko, F. Ricci, G. M. Rignanese, A. H. Romero, M. M. Schmitt, M. Torrent, M. J. van Setten, B. Van Troeye, M. J. Verstraete, G. Zérah, J. W. Zwanziger, *Comput. Phys. Commun.* **2020**, *248*, 107042.

[4]   S. Grimme, *J. Comput. Chem.* **2006**, *27*, 1787–1799.

[5]   H. Hövel, B. Grimm, B. Reihl, *Surf. Sci.* **2001**, *477*, 43–49.

[6]   K. M. Andrews, T. P. Pearl, *J. Chem. Phys.* **2010**, *132*, 214701

[7]   L. Feng, T. Wang, Z. Tao, J. Huang, G. Li, Q. Xu, S. L. Tait, J. Zhu*et*, *ACS Nano* **2019**, *13,* 10603–10611.

[8]   K. Greulich, A. Belser, D. Bischof, F. Widdascheck, M. S. Sättele, P. Grüninger, H. F. Bettinger, G. Witte, T. Chassé, H. Peisert, *ACS Appl. Electron. Mater.* **2021**, *3*, 825–837.

[9]   F. De Marchi, G. Galeotti, M. Simenas, E. E. Tornau, A. Pezzella, J. MacLeod, M. Ebrahimi, F. Rosei, *Nanoscale* **2018**, *10*, 16721–16729.

[10]  R. Y. Tay, H. Li, S. H. Tsang, M. Zhu, M. Loeblein, L. Jing, F. N. Leong, E. H.T. Teo, *Chem. Mater.* **2016**, *28*, 2180–2190.

[11]  M. Nishio, *Phys. Chem. Chem. Phys.* **2011**, *13*, 13873–13900.